Unsupervised anomaly detection in MeV ultrafast electron diffraction

Mariana A. Fazio,[1,*] Salvador Sosa Güitron,[1] Marcus Babzien,[2] Mikhail Fedurin,[2] Junjie Li,[2] Mark Palmer,[2] Sandra S. Biedron,[1,3] and Manel Martinez-Ramon[1]

[1] *Department of Electrical and Computer Engineering, University of New Mexico, New Mexico, USA*
[2] *Brookhaven National Laboratory, Upton, New York, USA*
[3] *Department of Mechanical Engineering, University of New Mexico, New Mexico, USA*

(Dated: May 21, 2025)

Abstract

arXiv:2505.13702v1 [cs.LG] 19 May 2025

I. INTRODUCTION

MeV ultrafast electron diffraction (MUED) is a pump-probe characterization technique for studying ultrafast processes in materials. The use of relativistic beams leads to decreased space-charge effects compared to typical ultrafast electron diffraction experiments employing energies in the keV range [1, 2]. Compared to other ultrafast probes such as X-ray free electron lasers, MUED has a higher scattering cross section with material samples and allows access to higher order reflections in the diffraction patterns due to the short electron wavelengths. However, this is a relatively young technology and several factors contribute to making it challenging to utilize, such as beam instabilities which can lower the effective spatial and temporal resolution.

In the past years, machine learning (ML) approaches to materials and characterization techniques have provided a new path towards unlocking new physics by improving existing probes and increasing the user's ability to interpret data. In particular, ML methods can be employed to control characterization probes in near-real time, acting as virtual diagnostics, or ML can be deployed to extract features and effectively denoise acquired data. In this later case, convolutional neural network architectures such as autoencoder models are an attractive and more powerful .. ML has yet to be applied to the MUED technique, where it can certainly enable advances that can further our understanding of ultrafast material processes in a variety of systems.

This study focus in the construction of an unsupervised anomaly detection methodology to detect faulty images in MUED. We believe that unsupervised techniques are the best choice for our purposes because the data used to train the detector does not need to be manually labeled, and instead, the machine is intended to detect by itself the anomalies in the dataset, which liberates the user of tedious, time-consuming initial image examination. The structure must, additionally, provide the user with some measure of uncertainty in the detection, so the user can take decisions based on this measure. If most images have a low uncertainty in the decision, the user may decide to manually examine a few images not confidently detected by the algorithm or directly throw them away to eliminate the associated risk of using them.

Non supervised methods can be roughly grouped in density-based, bagging, deep learning or kernel methods. The residual methods can use some of the above-mentioned techniques. Density based methods are those that estimate a compact observation model and from it a likelihood of these observations can be inferred. Then, the anomalous nature of a sample can be judged from this measure. In [3] histograms are used for this purpose and in [4] dissimilarity measures between samples are computed to determine whether a sample is an outlier or not. The k-nearest neighborhood strategy is used in [5, 6] to provide an approximate measure of likelihood. The bagging models use an ensemble of detectors constructed with bagging or data subsampling [7, 8].

In the field of deep learning we find methods that are also non-supervised and that are intended to process the data to reduce its dimensionality in what is called a bottleneck while preserving its distribution properties. These approaches are convenient when the dimension of the data is very high, as it is the case of images. The autoencoder model [9] is used for this purpose in [10, 11]. Generative adversarial networks [12] are applied for anomaly detection in [13].

Deep learning is useful when the number of data is high, but when the number of samples is low, we may take into consideration the use of kernel methods [14]. See, for example, the applications for outlier detection in [15] or [16]. The latter uses an autoencoder together with nonlinear dimensionality reduction with the help of kernel methods.

One of the most prominent kernel method for anomaly detection is perhaps the OC-SVM [17], that makes use of the maximum margin criterion [18], which effectively imposes a balance between the training error and the expressive capacity of the machine, reducing the overfitting when the number of samples is low. The OC-SVM is, besides, a non-supervised methodology. The Support Vector Data Description (SVDD) in [19] is based in the same criterion.

Residual methods are based on the examination of the prediction error over the sample under test. If a given variable that is observable can be inferred from the sample, then the prediction error can be measured. If the sample is anomalous, it is expected that it will produce a high error or residual. The determination of whether

* mfazio@unm.edu

the residual is high or not can be achieved by a model of the residual distribution (see, e.g. [20]).

Our approach combines the use of an autoencoder and a residual method. Indeed, the method encodes and reconstructs the images with the help of a convolutional autoencoder (CAE) [21] and then, the reconstruction error is used as a residual to estimate the posterior probability of that the image is normal conditional to the observed error. The error is modeled in a probabilistic way using a convex combination of distributions that automatically capture the conditional distribution of the error under the hypothesis of normal or fault.

II. EXPERIMENTAL METHODS

The MUED instrument is located in the Accelerator Test Facility at Brookhaven National Laboratory. A schematic representation of the experimental setup is presented in Fig. 1. The femtosecond electron beams are generated using a frequency-tripled Ti:Sapphire laser that illuminates a copper photocathode generating a high brightness beam. The electrons are then accelerated and compressed in a 1.6-cell RF cavity achieving energies up to 5 MeV. Current parameters of the electron beam source optimized for stability are presented in Table I. The sample chamber is located downstream from the source with a motorized holder for up to nine samples with cryogenic cooling capabilities and a window to allow laser pumping of the material. Next to the chamber a RF deflecting cavity is located and 4 m downstream the detector system is placed to collect the diffraction patterns. The detector consists of a phosphor screen followed by a copper mirror (with a hole for non-diffracted electrons to pass) and a CCD Andor camera of 512 pixels x 512 pixels with a large aperture lens. Suitable material systems for MUED require careful preparation with typical lateral sizes of 100 - 300 μm and roughly ¡ 100 nm thickness to assure electron transparency. Laser fluency is adjusted to avoid radiation-induced damage of the probed material.

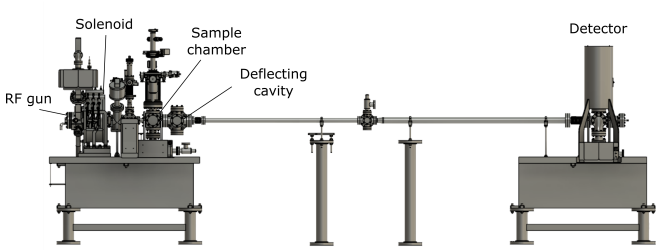

FIG. 1: Schematic representation of the experimental setup for the MUED instrument located in the Accelerator Test Facility at Brookhaven National Laboratory.

In the present study, electron diffraction patterns were measured for a thin single crystal Ta_2NiSe_5 sample. No pump laser was employed and single shot diffraction patterns were captured. Figure 2(a) shows a typical diffraction pattern measured for Ta_2NiSe_5 consisting of a grayscale image of 512 x 512 pixels. Figures 2(b)-(d) present different types of anomalies due to instabilities in the electron beam. A typical dataset will contain between 70 - 90 single shot diffraction patterns, including such anomalies that will affect the accuracy of the experiment. For this work, several datasets were captured during multiple days of operation of the MUED experiment employing the Ta_2NiSe_5 sample.

TABLE I: MUED source parameters for typical operation

Beam energy	3 MeV
Number of electrons per pulse	1.25×10^6
Temporal resolution	180 fs
Beam diameter	100 - 300 μm
Repetition rate	5 - 48 Hz
Number of electrons per sec per μm^2	88 - 880

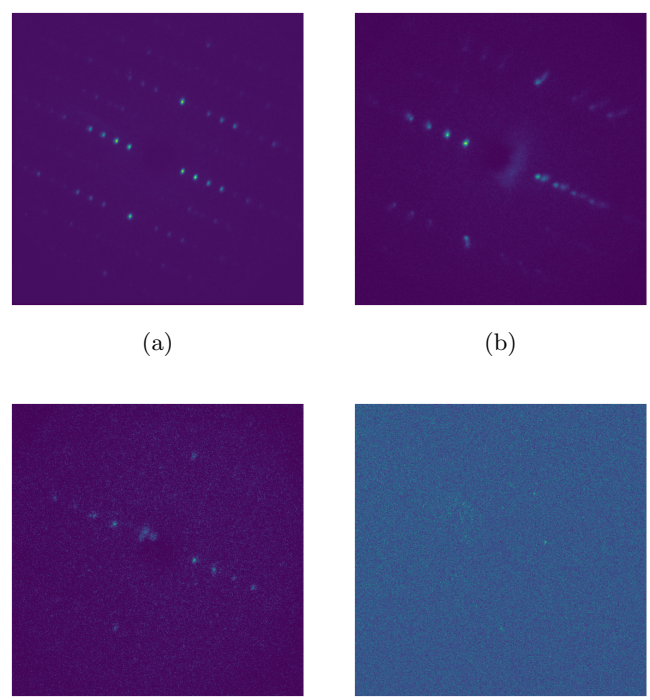

FIG. 2: Single shot diffraction patterns obtained for Ta_2NiSe_5: (a) typical diffraction pattern and (b) - (d) anomalous patterns.

III. COMPUTATIONAL METHODS

A. Data pre-processing procedure

As can be observed in figure 2, a diffraction pattern for a single crystal material consists of mostly background superimposed with discrete Bragg peaks. In order for the model to learn effectively the features of interested of the diffraction patterns, input patterns should consist mostly of signal (Bragg peaks) with minimal background. Therefore, pre-processing is a key step for ensuring good performance of the models for reconstruction of the diffraction patterns.

Each input pattern was normalized and divided in overlapping tiles of 80 x 80 pixels. Tiles containing only background were filtered out of the dataset. Tiles were defined as background if they contained white noise, and to evaluate this we applied the concept of spectral inverse participation ratio ($sIPR$). Given an image, we can classify it as white noise if it has a flat spatial spectral density. For simplicity, let's evaluate the frequency distribution in one dimension with $f_i(x)$ the contribution to the i-th frequency. If this distribution is normalized, we define the $sIPR$ as:

$$sIPR = \sum_{i=1}^{N} f_i^2(x) \tag{1}$$

with N the total number of discreet frequencies present in the image. If the distribution is consistent with white noise then $f_i(x)$ is equal for all frequencies and it follows that:

$$sIPR_{white-noise} = \frac{1}{N} \tag{2}$$

which is also the lowest possible value of the $sIPR$. Therefore, if a tile is found to have $sIPR > sIPR_{white-noise}$ it is included in the dataset. A slightly more restrictive threshold was adopted to limit those tiles with low signal-to-noise ratio with $sIPR > \frac{1.009}{N}$ being the condition for tiles to be included in the dataset.

This pre-processing procedure also served as a data augmentation technique and to decrease the computational cost of the calculations.

B. Convolutional autoencoder for reconstruction

A CAE has been used as the main element of the system. A schematic of the CAE model used for reconstruction of the diffraction patterns can be found in Fig. 3 and the full structure and parameters are presented in Table II. The parameters of the CAE have been cross-validated with the use of a set of normal images.

The CAE features a total of 6 layers and the output of the enconder (the feature vector) contains 256 components. For the encoder, each layer consists of a 2D convolution operation [22]. For convolution layer ℓ with $C_{\ell-1}$ input channels and C_ℓ output channels, the operation can be written as

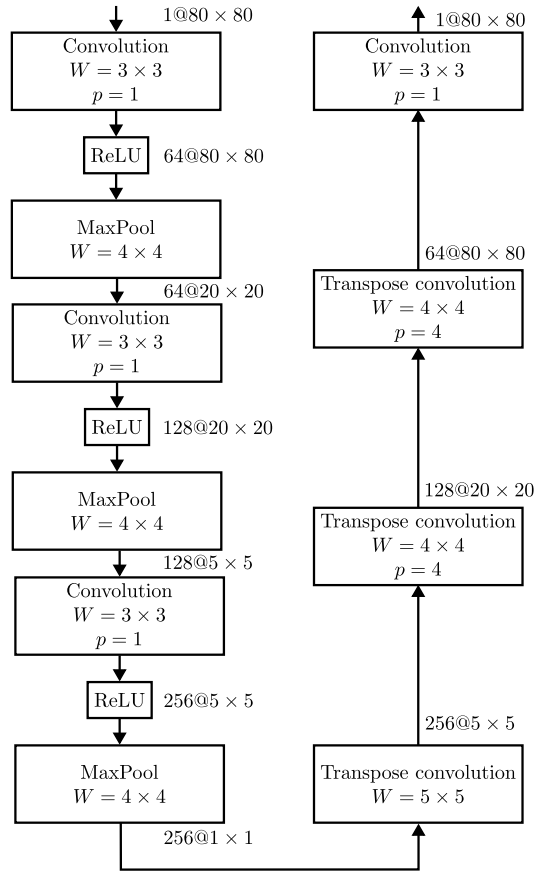

FIG. 3: Structure of the used convolutional encoder. The input is a tile of an image, with dimensions 80 × 80 for the present application, and the output is the reconstructed image contained in the tile.

Layer	Output shape	Parameters
Input	(80, 80, 1)	0
Conv2D + ReLu	(80, 80, 64)	640
MaxPool2D	(20, 20, 64)	0
Conv2D + ReLu	(20, 20, 128)	73,856
MaxPool2D	(5, 5, 128)	0
Conv2D + ReLu	(5, 5, 256)	295,168
MaxPool2D	(1, 1, 256)	0
ConvTranspose2D + ReLu	(5, 5, 256)	1,638,400
ConvTranspose2D + ReLu	(20, 20, 128)	524,288
ConvTranspose2D + ReLu	(80, 80, 64)	131,072
Conv2D	(80, 80, 1)	576

TABLE II: Structure and number of parameters of the convolutional autoenconder employed for reconstruction of the diffraction patterns.

$$\mathbf{Z}_j^\ell = \sum_{i=1}^{C_{\ell-1}} \mathbf{W}_{i,j}^\ell * \mathbf{H}_i^{\ell-1} + \mathbf{B}_j^\ell, \quad 1 \leq j \leq C_\ell \tag{3}$$

This is, each one of the channels $\mathbf{H}_i^{\ell-1}$ of the previous layer is convolved with convolution kernel $\mathbf{W}_{i,j}^\ell$ and then added together. Then a matrix $\mathbf{B}_j^\ell$ of bias values is added to produce the output $\mathbf{Z}_j^\ell$ of channel j in later ℓ.

This image is then zero padded, this is, a number p of rows containing zeros are added at the left and right and to top and bottom of the image.

This output is then passed through a nonlinear transformation with two steps, a nonlinear activation and a MaxPooling [23, 24] to produce output channel $\mathbf{H}_j^\ell$, that will be summarized detailed further.

The first convolution layer has 64 output channels and the size of each channel is 80×80. The convolution kernel is 3×3 and a zero padding of one pixel is applied to each edge of the resulting image. Therefore, the convolution output has a width and height of $80 - 3 + 1 = 78$. Due to the zero padding, the dimension is increased to 80. After that, a MaxPooling is applied with a window of dimensions 4×4. The MaxPooling consists of selecting the pixel with the maximum value inside a window of pixels, for all disjoint windows of the image. Therefore, the dimension of the resulting image is reduced by a factor 4 in each dimension. This results in a final dimension of 20×20 pixels. After this, a Rectified Linear Unit (ReLU) activation [25] is applied. The ReLU activation is the simplest nonlinear activation and it can be written as

$$\mathrm{ReLU}(z) = max(0, z)$$

this is, if the argument is negative, the output is zero, otherwise the output is equal to the input.

Following the same computations, the output of the last convolutional layer contains images of a single pixel. The number of channels at the output is 256. This is the so called bottleneck of the encoder, and it is intended to contain all the information needed to reconstruct the image.

For the decoder, each layer consists of a 2D transpose convolution operation [26] with a rectified linear unit activation that simultaneously increases the dimensionalty and decreases the channels in a similar manner to the layers of the encoder. The operation can be written as

$$\mathbf{Z}_j^\ell = \sum_{i=1}^{C_{\ell-1}} \mathbf{W}_{i,j}^\ell \otimes \mathbf{H}_i^{\ell-1} + \mathbf{B}_j^\ell, \quad 1 \leq j \leq C_\ell \tag{4}$$

In this operation, instead of a convolution, a Hadamard matrix product between the kernel and the image is applied. The dimension of the resulting image is equal to the product of the dimension of the input image times the dimension of the kernel. The first transpose convolution has a kernel of dimensions 5×5, and since the input has a single pixel, the resulting images have dimensions 5×5. The dimensionality is further increased with two more transpose convolutions up to $\times 80$ and 64 channels. In order to combine all the channels, a last convolution with a kernel of dimensions 4×4 and zero padding with $p = 1$ results in a single channel of dimension 80×80. The output layer is a 2D convolution operation with a linear activation.

The mean squared error (MSE) loss was used with an Adam optimizer and standard backpropagation.

C. Anomaly detection

The detection of anomalies is simply performed by the computation of the MSE error across all pixels of a reconstructed image. Low errors will correspond to normal images, and higher errors correspond to anomalies. The rational behind this strategy can be that the number of anomalous images during the training is negligible compared to the number of normal images. Then, the CAE can reconstruct these images, but the number of anomalies is too low for the CAE to be able to reconstruct them, since they are drawn from a different distribution. This anomaly detection method is known as residual analysis detection [27].

Another explanation for the behavior of the MSE error is that the CAE has enough expressive capacity to reconstruct normal images, but the anomalies introduce additional complexity in the images, which the CAE is not able to learn. So to speak, our model is purportedly *underfit* for the faulty images. In this case, the CAE can be trained with a significant number of anomalies, which will not affect the detection performance. There is an extensive scholarship in generalization bounds in deep learning (see, e.g. [28]) that treat the topic of overfitting and underfitting in neural networks.

If a significant number of anomalies are present in a dataset, the CAE will present a high training error in these images. In preliminary experiments, we observed that the errors group in two separate clusters, and therefore the likelihood function of these errors can be modeled with a mixture of probability density functions $p(e|N)$ and $p(e|A)$ [29], which are the likelihoods of the error under the hypothesis that the image is normal (N) or an anomaly (A). If the prior probability for these anomalies $p(A) = 1 - p(N)$, then a posterior probability can be written as

$$p(N|e) = \frac{p(e|N)p(N)}{p(e|A)p(A) + p(e|N)p(N)} \tag{5}$$

It has been experimentally shown that the marginal likelihood of the MSE error

$$p(e) = p(e|A)p(A) + p(e|N)p(N) \tag{6}$$

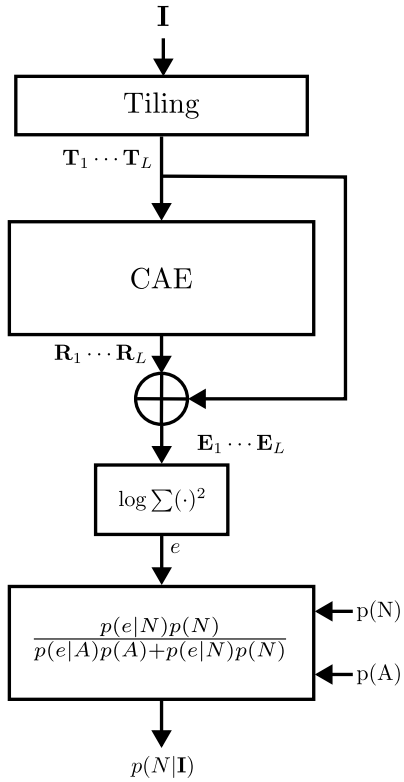

FIG. 4: Structure of the detector.

can be modeled with two Gamma distributions or two Rice distributions as conditional likelihoods. If it is assumed that a significant number of anomalies is present in a dataset, but they are not previously detected, as it is the case of this work, both the parameters of the distributions and the values of priors $p(N)$ and $p(A)$ can be easily adjusted by the use of the ME algorithm or by using the limited memory Broyden–Fletcher–Goldfarb–Shanno with box constraints (L-BFGS-B) [30] algorithm. Once the posterior probability is estimated, the detector provides the user with an estimation of the probability that the sample is normal. That way, those samples that have a probability close to 0.5 can be visually analyzed by the user.

The process is visualized in Fig. 4. The process starts with the introduction of an image, which is tiled. Each of the tiles $\mathbf{T}_i$ is reconstructed and its reconstruction error $\mathbf{E}_i$ is computed. The, the logarithm of the mean square error across all the pixels of the tiles is computed and with it, an estimation of the posterior $p(N|e) = p(N|\mathbf{I})$ is computed. In the system, it is assumed that both likelihoods and the priors are estimated. The details of the particular algorithm for this estimation are provided in the next section.

Moreover, a threshold can be established by finding the value of the error e that gives a certain probability, for example, 0.5. The threshold can be used to classify the samples with a reasonable balance between probability of detection and probability of false alarm.

D. Computational resources

The experiments were run in the Center for Advanced Research Computiing (CARC) Supercomputer of the University of New Mexico. The used resources were a SGI AltixXE Xeon X5550 at 2.67 GHz, with Intel Xeon Nehalem EP architecture. A total of 8 nodes with 8 cores each were used. The operating system was Linux CentOS 7. The programming language was Python 3 and the convolutional autoencoder was programmed using the Pytorch library.

IV. EXPERIMENTS

A. Training and test of the autoencoder

The autoencoder has been trained with 6537 tiles corresponding to 100 images. The machine is agnostic about which images are faulty. The training algorithm is the standard Adam with MMSE criterion. The training parameters are: $\mu = 0.01$, batch size equal to 32, and 10 training epochs. The total training time was of 17 minutes. An example of the reconstruction for 10 arbitrary normal tiles of an image is shown in Fig. 5

During the test, each image is segmented in tiles, and passed to the autoencoder. The mean squared error is computed across all pixels of all tiles of the image.

The CAE was tested with the available 1521 images (including the training ones), of which 615 (40.4%) of them were faulty images, and 906 were normal. The total number of analyzed tiles is about 10^5. The total test time was of 24 minutes, corresponding roughly to 1 second per image. This includes the image loading from the hard drive, which took most of the processing time. The logarithm of the MSE across all pixels of each tested image can be seen in Fig. 6.

B. Statistical analysis of the reconstruction error

In order to estimate the marginal likelihood of the error, both conditional likelihoods have been modeled with two Rice distributions with the form

$$p(e|H) = \frac{2(e-\mu)}{\alpha} \exp\left(\frac{-((e-\mu_H)^2 + \nu_H^2)}{\alpha_H}\right) \cdot \cdot I_0\left(\frac{2(e-\mu_H)\nu_H}{\alpha_H}\right) \tag{7}$$

where parameters μ_H, ν_H and α_H are the bias, shape and scale of the distributions, for hypothesys $H = A$ (anomaly) and $H = N$ (normal). The L-BFGS-B algorithm is used to minimize the negative log likelihood

$$NLL = -\sum_{i=0}^{N-1} \log\left(wp(e_i|N) + (1-w)p(e_i|A)\right) \tag{8}$$

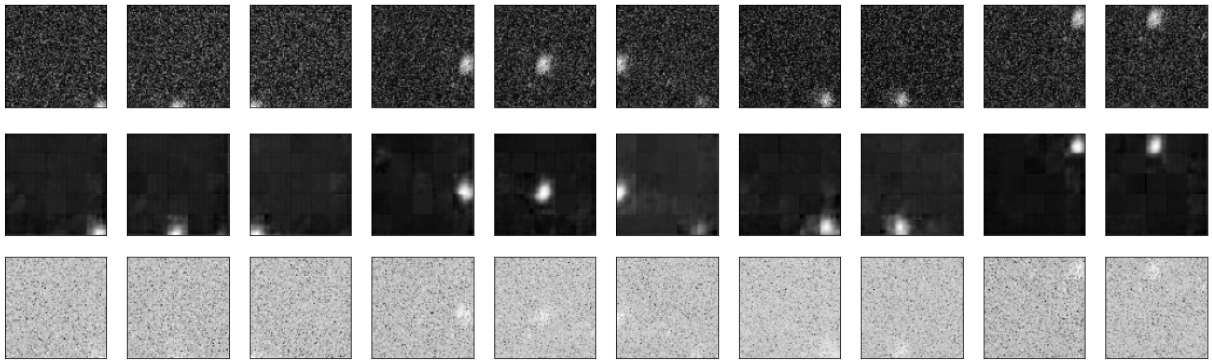

FIG. 5: Comparison between 10 original and reconstructed test tiles of an image and their corresponding reconstruction error. The graphs show the logarithm of the amplitudes and the squared error.

.

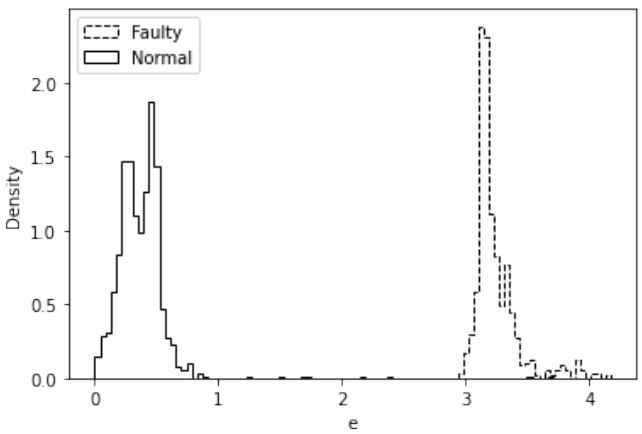

FIG. 6: Histogram of the logarithm of the MSE of the reconstruction error for all the available images.

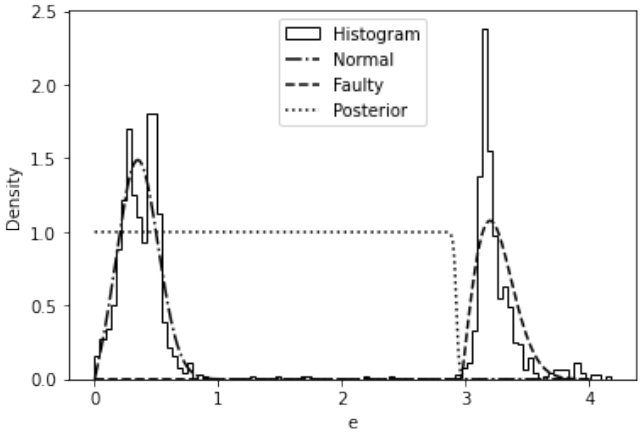

FIG. 7: Results of the statistical analysis. The lines labelled as Normal and Faulty represent the estimated likelihoods of both hypotheses weighted times the corresponding priors. The line labelled as posterior corresponds to $p(N|e)$

.

with respect to parameters $w, \mu_N, \nu_N, \alpha_N, \mu_N, \nu_N, \alpha_N$, where w plays the role of the prior $p(N)$. In order to add robustness to the optimization, we apply a simulated annealing to the optimization. This is, we start by initializing the 7 parameters at random, and run an optimization. We repeat the optimization 100 times, and keep the optimized values that provide the 10 lowest values of the negative log likelihood. Then we generate 10 random parameter sets around these values, run the optimization with them as initial values, keep the 10 best results and iterate the process until convergence.

Fig. 7 shows the result of the statistical analysis after this optimization, where both joint probability estimations $p(e, H) = p(H)p(e|H)$ are represented in a dash-dotted line for $H = N$ and in a dashed line for $H = A$. The optimized values for the parameters were $\nu_N = 1.82, \mu_N = 0, \alpha_N = 0.17, \nu_A = 0, \mu_A = 2.94, \alpha_A = 0.25, w = 0.6$. Note here that for the case of faulty images (H=A), the shape parameter ν_A is zero, and therefore the distribution becomes a biased Rayleigh distribution. The distribution for the normal images is not biased ($\mu_N = 0$). Finally, the prior of the normal images is $p(N) = w = 0.6$, as expected since this is the fraction of normal images in the dataset.

C. Estimation of the detection threshold

In order to estimate the detection threshold we simply establish a minimum posterior probability for the normal images of 50%. The MSE corresponding to this can be computed by using Eq. (5) with Eq. (7) and the optimized parameters. For the above experiment this threshold is $e_t = 2.925$.

In order to determine the quality of the threshold, the Receiver Operating Curve (ROC) has been computed for different detection thresholds ranging from 0 to 5. This curve shows the relationship between the fraction of true positive detections and false positive detections for all the thresholds in the range. The graphic has been zoomed

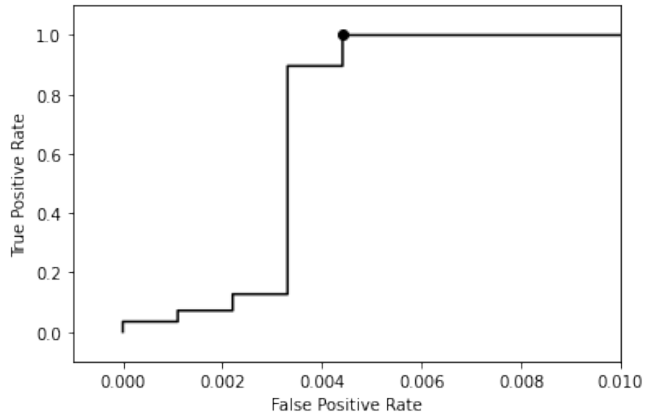

FIG. 8: ROC curve for various values of the detection threshold. The dot corresponds to the automatically chosen value of the threshold, with a 100% of detections and a false positive rate of 4.4×10^{-3}.

for a false positive rate between 0 and 10^{-2}. The result of the threshold chosen with the algorithm above is marked with a dot in the figure, and it shows a detection rate of 1, and a false positive rate of 4.4×10^{-3}. The errors correspond to 4 normal data whose estimation error is high.

D. Experiment with reduced number of anomalies

In order to show the robustness of the method, the test is repeated with a reduced number of faulty images. The dataset used contains now the same number of normal images but only 30 faulty images chosen at random, so the proportion of normal to faulty images is now 98% of normal to 2% of faulty images. The experiment is repeated to compute the new distributions and automatic threshold.

Fig. 9 shows the result of the experiment. The left pane shows the histogram of the error, where the faulty images are now a small cluster. The estimated likelihoods are visually in agreement with the histograms. The posterior probability is also represented. The right pane shows the ROC with the point automatically selected, showing a false positive rate of 2.2×10^{-3} or 0.22%.

In this case, the optimized values for the parameters were $\nu_N = 1.81, \mu_N = 0, \alpha_N = 0.17, \nu_A = 0, \mu_A = 3, \alpha_A = 0.23, w = 0.97$. These values are in high agreement with the previous ones, but the prior $p(N)$ represented by variable w is 0.97, in agreement with the fraction of faulty data.

V. CONCLUSIONS

We presented a methodology for anomaly detection applied to detecting of faulty images that is fully unsupervised. This is, the system is not provided with any information about what images are normal or faulty, which allows the user to train the method without the necessity of labelling the training images as normal or faulty. This way, the method can be trained and tested with a high number of images in short time.

The method provides the user with a an estimation of the probability of that the image is normal. This informs the user about the images that are difficult to classify for them to visually inspect a posterior. The detection threshold is computed automatically using a set of validation images that do not need to be labelled either, which makes this system fully flexed and totally autonomous, freeing the user of manually adjusting any parameters of the detector.

The methodology has been trained with only 100 images. The test images were 1521, that were used first to estimate the threshold. After this, these images were tested to detect the faulty ones, with a false positive rate that ranged between 0.2 and 0.4%. The training time was of about 10 seconds per image, and the test time was of about one second per image.

ACKNOWLEDGMENTS

We would like to thank the UNM Center for Advanced Research Computing, supported in part by the National Science Foundation, for providing the high performance computing, large-scale storage, and visualization resources used in this work.

We wish to acknowledge the support of

[1] X. Wang, Z. Wu, and H. H. Ihee, Femto-seconds electron beam diffraction using photocathode rf gun, in *Proceedings of the 2003 particle accelerator conference*, Vol. 1 (IEEE, 2003) pp. 420–422.

[2] P. Zhu, Y. Zhu, Y. Hidaka, L. Wu, J. Cao, H. Berger, J. Geck, R. Kraus, S. Pjerov, Y. Shen, *et al.*, Femtosecond time-resolved mev electron diffraction, New Journal of Physics **17**, 063004 (2015).

[3] M. Goldstein and A. Dengel, Histogram-based outlier score (hbos): A fast unsupervised anomaly detection algorithm, KI-2012: Poster and Demo Track , 59 (2012).

[4] M. M. Breunig, H.-P. Kriegel, R. T. Ng, and J. Sander, Lof: identifying density-based local outliers, in *Proceedings of the 2000 ACM SIGMOD international conference on Management of data* (2000) pp. 93–104.

[5] S. Ramaswamy, R. Rastogi, and K. Shim, Efficient algorithms for mining outliers from large data sets, in *Proceedings of the 2000 ACM SIGMOD international conference on Management of data* (2000) pp. 427–438.

[6] F. Angiulli and C. Pizzuti, Fast outlier detection in high

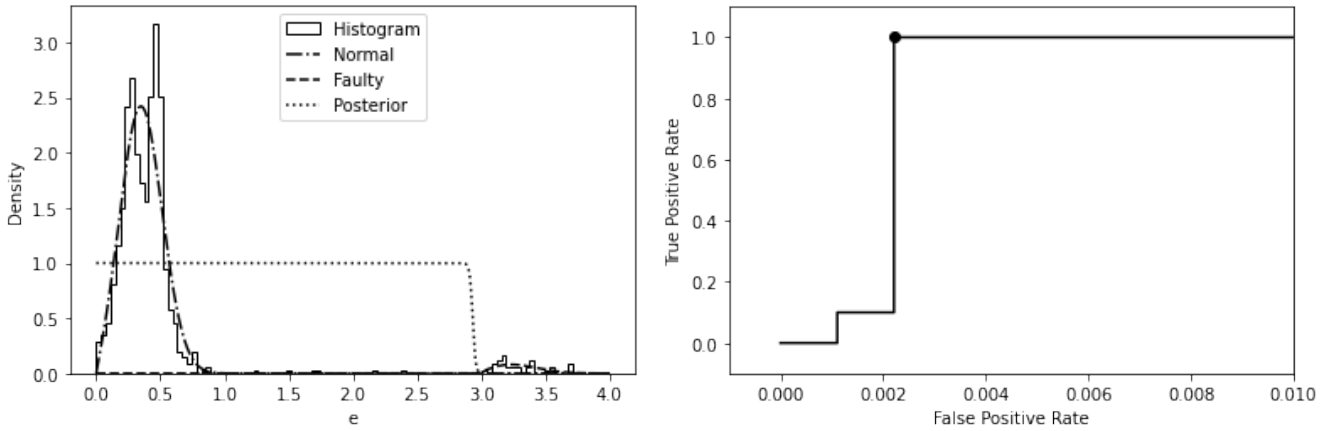

FIG. 9: Results of an automatic threshold estimation with a 98% of normal images and a 2% of faulty images. The dot in the left pane shows the result of the true positive rate as a function of the true positive rate for the estimated threshold. The false positive rate in this case is of 2.2×10^{-3}.

dimensional spaces, in *European conference on principles of data mining and knowledge discovery* (Springer, 2002) pp. 15–27.

[7] A. Lazarevic and V. Kumar, Feature bagging for outlier detection, in *Proceedings of the eleventh ACM SIGKDD international conference on Knowledge discovery in data mining* (2005) pp. 157–166.

[8] C. C. Aggarwal and S. Sathe, Theoretical foundations and algorithms for outlier ensembles, Acm sigkdd explorations newsletter **17**, 24 (2015).

[9] G. E. Hinton and R. R. Salakhutdinov, Reducing the dimensionality of data with neural networks, science **313**, 504 (2006).

[10] M. Sakurada and T. Yairi, Anomaly detection using autoencoders with nonlinear dimensionality reduction, in *Proceedings of the MLSDA 2014 2nd workshop on machine learning for sensory data analysis* (2014) pp. 4–11.

[11] J. Chen, S. Sathe, C. Aggarwal, and D. Turaga, Outlier detection with autoencoder ensembles, in *Proceedings of the 2017 SIAM international conference on data mining* (SIAM, 2017) pp. 90–98.

[12] I. Goodfellow, J. Pouget-Abadie, M. Mirza, B. Xu, D. Warde-Farley, S. Ozair, A. Courville, and Y. Bengio, Generative adversarial networks, Communications of the ACM **63**, 139 (2020).

[13] Y. Liu, Z. Li, C. Zhou, Y. Jiang, J. Sun, M. Wang, and X. He, Generative adversarial active learning for unsupervised outlier detection, IEEE Transactions on Knowledge and Data Engineering **32**, 1517 (2019).

[14] J. Shawe-Taylor, N. Cristianini, *et al.*, *Kernel methods for pattern analysis* (Cambridge university press, 2004).

[15] J. Hardin and D. M. Rocke, Outlier detection in the multiple cluster setting using the minimum covariance determinant estimator, Computational Statistics & Data Analysis **44**, 625 (2004).

[16] M.-L. Shyu, S.-C. Chen, K. Sarinnapakorn, and L. Chang, *A novel anomaly detection scheme based on principal component classifier*, Tech. Rep. (Dept. of Electrical and Computer Engineering, Miami University, Coral Gables, FL, 2003).

[17] B. Schölkopf, J. C. Platt, J. Shawe-Taylor, A. J. Smola, and R. C. Williamson, Estimating the support of a high-dimensional distribution, Neural computation **13**, 1443 (2001).

[18] V. Vapnik, *The nature of statistical learning theory* (Springer science & business media, 2013).

[19] D. M. Tax and R. P. Duin, Support vector data description, Machine learning **54**, 45 (2004).

[20] A. S. Zamzam, X. Fu, and N. D. Sidiropoulos, Data-driven learning-based optimization for distribution system state estimation, IEEE Transactions on Power Systems **34**, 4796 (2019).

[21] X. Mao, C. Shen, and Y.-B. Yang, Image restoration using very deep convolutional encoder-decoder networks with symmetric skip connections, Advances in neural information processing systems **29** (2016).

[22] J. Gu, Z. Wang, J. Kuen, L. Ma, A. Shahroudy, B. Shuai, T. Liu, X. Wang, G. Wang, J. Cai, *et al.*, Recent advances in convolutional neural networks, Pattern recognition **77**, 354 (2018).

[23] K. Fukushima and S. Miyake, Neocognitron: A new algorithm for pattern recognition tolerant of deformations and shifts in position, Pattern recognition **15**, 455 (1982).

[24] Y. LeCun, L. Bottou, Y. Bengio, and P. Haffner, Gradient-based learning applied to document recognition, Proceedings of the IEEE **86**, 2278 (1998).

[25] V. Nair and G. E. Hinton, Rectified linear units improve restricted boltzmann machines, in *Proceedings of the 27th international conference on machine learning (ICML-10)* (2010) pp. 807–814.

[26] V. Dumoulin and F. Visin, A guide to convolution arithmetic for deep learning, arXiv preprint arXiv:1603.07285 (2016).

[27] I. Hwang, S. Kim, Y. Kim, and C. E. Seah, A survey of fault detection, isolation, and reconfiguration methods, IEEE transactions on control systems technology **18**, 636 (2009).

[28] Y. Cao and Q. Gu, Generalization bounds of stochastic gradient descent for wide and deep neural networks, Advances in neural information processing systems **32** (2019).

[29] K. P. Murphy, *Machine learning: a probabilistic perspec-*

tive (MIT press, 2012).

[30] R. Fletcher, *Practical methods of optimization* (John Wiley & Sons, 2000).